ELSEVIER

Contents lists available at ScienceDirect

Journal of Computational Physics

journal homepage: www.elsevier.com/locate/jcp



A Chebyshev-based rectangular-polar integral solver for scattering by geometries described by non-overlapping patches

Oscar P. Bruno^{a,*}, Emmanuel Garza^{a,1}

^aComputing and Mathematical Sciences, Caltech, 1200 E California Blvd, Pasadena CA 91125, United States

ARTICLE INFO

Article history:
Received August 22, 2020
Received in final form August 22, 2020
Accepted August 22, 2020
Available online August 22, 2020

ABSTRACT

This paper introduces a high-order-accurate strategy for integration of singular kernels and edge-singular integral densities that appear in the context of boundary integral equation formulations for the problem of acoustic scattering. In particular, the proposed method is designed for use in conjunction with geometry descriptions given by a set of arbitrary non-overlapping logicallyquadrilateral patches—which makes the algorithm particularly well suited for computer-aided design (CAD) geometries. Fejér's first quadrature rule is incorporated in the algorithm, to provide a spectrally accurate method for evaluation of contributions from far integration regions, while highly-accurate precomputations of singular and near-singular integrals over certain "surface patches" together with two-dimensional Chebyshev transforms and suitable surface-varying "rectangular-polar" changes of variables, are used to obtain the contributions for singular and near-singular interactions. The overall integration method is then used in conjunction with the linear-algebra solver GMRES to produce solutions for sound-soft open- and closed-surface scattering obstacles, including an application to an aircraft described by means of a CAD representation. The approach is robust, fast, and highly accurate: use of a few points per wavelength suffices for the algorithm to produce far-field accuracies of a fraction of a percent, and slight increases in the discretization densities give rise to significant accuracy improvements.

© 2020 Elsevier Inc. All rights reserved.

1. Introduction

The solution of scattering problems by means of boundary integral representations has proven to be a game-changer when the ratio of volume to surface scattering is large, where volumetric solvers become intractable due to memory requirements and computational cost. At the heart of every boundary integral equation (BIE) solver lies an integration strategy that must be able to handle the weakly singular integrals associated with the integral formulations

^{*}Corresponding author: Tel.: +0-000-000-0000; fax: +0-000-000-0000; e-mail: obruno@caltech.edu (Oscar P. Bruno), emmanuel.garza@caltech.edu (Emmanuel Garza)

of e.g. acoustic and electromagnetic scattering. Several approaches have been proposed to deal with this difficulty, most notably those put forward in [1, 2, 3, 4, 5, 6].

For the problem of scattering by two-dimensional surfaces in three-dimensional space, which reduces to two-dimensional weakly-singular integral equations over the scatterer's surface, there is no simple high-order quadrature rule of the type put forth in [7, 8, 9] for evaluation of weakly-singular operators associated with curves in two-dimensional space. This makes the three-dimensional problem considerably more difficult than its two dimensional counterpart. Therefore, a number of approaches have been proposed—including, notably, Nyström, collocation and Galerkin methodologies—for the evaluation of integral operators over two-dimensional surfaces. Nyström methods use a quadrature rule to evaluate integrals from a point-mesh discretization, with testing on the set of integration points; the collocation approach finds a solution on a finite-dimensional space which satisfies the continuous BIE at a set of collocation points; the Galerkin approach solves the BIE in a discrete weak form, using finite-element spaces for both solution representation and testing.

In this contribution a Nyström method is presented in which, as in [10], the far interactions are computed via Fejér's first quadrature rule, which yields spectrally accurate results for smooth integrands, while the integrals involving singular and near-singular kernels are obtained by relying on highly-accurate precomputed integrals (which are produced by means of rectangular-polar changes of variables that vary with the observation point) of the kernels times Chebyshev polynomials, together with Chebyshev expansions of the densities. The derivatives of the rectangular-polar change of variables vanish at the kernel-singularity and geometric-singularity points, producing respectively "floating" and fixed clustering around those points, and thus giving rise to high-order accuracy. The floating changes of variables are analogous to those in the polar integration method [1], but differs in the fact that it is applied on a rectangular mesh, hence the "rectangular-polar" terminology we use. The *sinh* transform [11, 12] was also tested as an alternative to the change of variables we eventually selected: the latter method was preferred as the *sinh* change of variables does not appear to allow sufficient control on the distribution of discretization points along the integration mesh, which is needed in order to accurately resolve the wavelength without use of an excessively fine discretization mesh near singularities.

The proposed rectangular-polar approach, which yields high-order accuracy, leads to several additional desirable properties. The proposed use of Chebyshev representations for the density, for example, allows for the evaluation of differential geometry quantities needed for electromagnetic BIE by means differentiation of corresponding Chebyshev series. Additionally, the nodes for Fejér's first quadrature are the same as the nodes for the discrete orthogonality property of Chebyshev polynomials, which make the computation of the Chebyshev transforms straightforward. In addition to scattering by a bounded obstacle, this integral equation solver can also be used in the context of the Windowed Green function method for scattering by unbounded obstacles such as layered media [13, 14, 15] and waveguides [16].

The present paper demonstrates the effectiveness of the integration strategy through a variety of numerical examples. Although a convergence analysis of the methodology is not presented here, we suggest that a framework related to that of [17] (which does establish the stability and convergence of a Nyström integral-equation method based on use of Fourier spectral expansions, albeit in a context characterized by use of overlapping patches and partitions of unity), could be employed to analyze the stability and convergence of the present approach.

This paper is organized as follows. After basic preliminaries are put forth in Section 2, the proposed surface representation structure is described in Section 3. The overall rectangular-polar integration strategy, including details concerning the methodologies used to produce integrals for smooth, singular and near-singular kernels as well as edge-singular integral densities, is presented in Section 4. A variety of numerical results for open and closed scattering surfaces are then presented in Section 5, emphasizing the convergence properties of both the forward map (which evaluates the action of the integral operator for a given density) as well as the full scattering solver, and demonstrating the accuracy, generality, and speed of the proposed approach. Results of an application to a problem of scattering by a geometry generated by CAD software is also presented in that section, demonstrating the applicability of the proposed method to complex geometrical designs in science and engineering. Section 6, finally, presents a few concluding remarks.

2. Preliminaries

For conciseness, we consider the problem of acoustic scattering by a sound-soft obstacle, though the methodology proposed is also applicable to electromagnetic scattering and other integral-equation problems involving singular

kernels.

Let Ω denote the complement of an obstacle D in three-dimensional space, let Γ denote the boundary of the obstacle, and call U^{inc} , U^{scat} and $U = U^{\text{scat}} + U^{\text{inc}}$ the incident, scattered and total fields, respectively. Then, the total field $U = U^{\text{scat}} + U^{\text{inc}}$ satisfies the Helmholtz equation

$$\Delta U(\mathbf{r}) + k^2 U(\mathbf{r}) = 0, \quad \mathbf{r} \in \mathbb{R}^3 \setminus \overline{\Gamma}, \tag{1}$$

with wavenumber $k = 2\pi/\lambda$, and the scattered field U^{scat} satisfies the Sommerfeld radiation condition as well as the boundary condition

$$U^{\text{scat}}(\mathbf{r}) = -U^{\text{inc}}(\mathbf{r}), \quad \mathbf{r} \in \Gamma.$$
 (2)

As is well known [9], the scattered field can be represented in terms of layer potentials—which reduce the scattering problem to a boundary integral equation that contains singular kernels. The single- and double-layer potentials are defined by

$$\mathscr{S}[\widetilde{\varphi}](r) = \int_{\Gamma} G(r, r') \widetilde{\varphi}(r') d\sigma(r'), \quad r \in \mathbb{R}^3 \setminus \overline{\Gamma},$$
(3)

$$\mathscr{D}[\widetilde{\varphi}](r) = \int_{\Gamma} \frac{\partial G(r, r')}{\partial n(r')} \widetilde{\varphi}(r') d\sigma(r'), \quad r \in \mathbb{R}^3 \setminus \overline{\Gamma},$$
(4)

respectively, where $G(\mathbf{r}, \mathbf{r}') = \exp{(ik|\mathbf{r} - \mathbf{r}'|)}/4\pi|\mathbf{r} - \mathbf{r}'|$ is the free-space Green function of the Helmholtz equation, \mathbf{n} is the outward-pointing normal vector, and $\widetilde{\varphi}$ is the surface density.

In this paper, we demonstrate the proposed methodology through applications to two main scattering problems under a unified scheme, namely, the problems of scattering by closed and open surfaces. These two important scattering problems are briefly described in the following two sections.

2.1. Closed surfaces

For the case of a closed, bounded obstacle, we use a standard combined-field formulation [9]

$$U^{\text{scat}}(\mathbf{r}) = \mathcal{D}[\widetilde{\varphi}](\mathbf{r}) - ik\mathcal{S}[\widetilde{\varphi}](\mathbf{r}), \quad \mathbf{r} \in \mathbb{R}^3 \setminus \overline{\Gamma}, \tag{5}$$

which leads to the second-kind integral equation at the boundary

$$\frac{1}{2}\widetilde{\varphi}(\mathbf{r}) + D[\widetilde{\varphi}](\mathbf{r}) - ikS[\widetilde{\varphi}](\mathbf{r}) = -U^{\text{inc}}(\mathbf{r}), \quad \mathbf{r} \in \Gamma,$$
(6)

where the single- and double-layer boundary operators are defined as

$$S[\widetilde{\varphi}](r) = \int_{\Gamma} G(r, r') \widetilde{\varphi}(r') d\sigma(r'), \quad r \in \Gamma,$$
(7)

$$D[\widetilde{\varphi}](r) = \int_{\Gamma} \frac{\partial G(r, r')}{\partial n(r')} \widetilde{\varphi}(r') d\sigma(r'), \quad r \in \Gamma,$$
(8)

respectively.

This formulation is guaranteed to provide a unique density solution to the scattering problem considered here [9], and, owing in part, to the second-kind character of this integral equation (for smooth surfaces), and as illustrated in Table 2, the number of GMRES iterations required to attain a given residual for this equation remains essentially bounded as *k* is increased.

In the case where geometrical edges and corners are present, which we consider in Section 5.2, the double-layer operator is no longer compact [18, 19, 20], and hence the integral equation is not a second-kind equation. In Section 5.2 we present numerical evidence showing that, even in this case, the proposed integration technique can yield an accurate solution. For example, for the three-dimensional problem of scattering by a cube presented in 5.2, far-field errors better than 10^{-7} were achieved.

2.2. Open surfaces

The combined field formulation (5) is not applicable for problems of scattering by open surfaces—since, for example, the jump conditions for the double-layer potential over Γ imply different field values on the two sides of Γ , and, hence, this potential cannot satisfy a nontrivial Dirichlet boundary value problem on Γ . A single-layer formulation can be used for such purpose, however; in this case we have

$$U^{\text{scat}}(\mathbf{r}) = \mathcal{S}[\widetilde{\varphi}](\mathbf{r}), \quad \mathbf{r} \in \mathbb{R}^3 \setminus \overline{\Gamma}, \tag{9}$$

which, for the boundary conditions (2), leads to a first-kind integral equation

$$S[\widetilde{\varphi}](r) = -U^{\text{inc}}(r), \quad r \in \Gamma.$$
(10)

This is in fact the formulation recommended in [21] for the Dirichlet problem (see e.g. [Sec. 12]), even in presence of the better-conditioned but more expensive second-kind formulation introduced in that contribution. (In the Neumann case, which, for definiteness we do not consider here, the second-kind formulation is highly beneficial [21, Sec. 12].)

This paper utilizes the formulation (9), as recommended, but it adopts an alternative quadrature approach, which is based once again on the proposed rectangular-polar paradigm. An important aspect of the open-surface case is that the solution $\widetilde{\varphi}(\mathbf{r})$ is singular at the edge, with a singularity of the form

$$\widetilde{\varphi} \sim \frac{\Phi}{\sqrt{d}},$$
 (11)

where d is the distance to the edge and Φ is an infinitely differentiable function throughout the boundary, including the edge, as reviewed in [21]. In that paper, a strategy based on quadrature rules for the exact singularity form where introduced, together with the polar integration method [1]. We propose an alternative approach in which, in addition of the polar-rectangular setup, a change of variables is introduced in the parametrization of the surface, whose derivatives vanish at the edges and thus smoothens the integrands. Although not specifically tailored to the exact form of the singularity at open-surface edges, the proposed algorithm does provide a robust, highly-accurate, efficient and simple approach for the treatment of the density-singularities that arise for open surfaces—which, importantly, applies seamlessly to the closed-surface edge case, for which the degree of the singularity depends on the edge angle, which may itself vary along the edge.

3. Surface representation

The proposed method assumes the scattering surface, whether closed or open, is described by a set of M non-overlapping "logically-quadrilateral" (LQ) parametrized patches. This geometrical description is particularly well suited for designs generated by CAD software, which generally can export surface representations in terms of NURBS-based models—that is, parametrizations expressed in terms of certain types of Rational B-Splines. In fact, the potential afforded by direct use of CAD-exported representations (without the expense, difficulty and accuracy deterioration inherent in the use of surface triangulations) provided the driving force leading to this paper: each NURBS trimmed surface can be "quadrilateralized" without great difficulty, which lends the method essentially complete geometric generality and a remarkable ease of use.

In the proposed approach, then, the scattering surface Γ is partitioned on the basis of a finite number M of parametrizations

$$\tilde{r}^q: [-1,1]^2 \to \mathbb{R}^3 \quad (q=1,2,\ldots,M),$$

each one of which maps the unit square $[-1, 1]^2$ in the (s, t)-plane onto an LQ patch within Γ . Since we require the system of LQ patches to cover Γ , we have, in particular

$$\Gamma = \bigcup_{q=1}^{M} \Gamma^{q} \quad \text{where} \quad \Gamma^{q} = \left\{ \widetilde{\boldsymbol{r}}^{q}(s,t) \mid (s,t) \in [-1,1]^{2} \right\}. \tag{12}$$

Clearly, any r-dependent combination I = I(r) of integrals over Γ , of the types considered in Sections 2.1 and 2.2, can be decomposed as a sum of integrals $I^q(r)$ over the various patches. In particular, the integral representations and

boundary operators considered in those sections can be expressed in the form

$$I(\mathbf{r}) = \sum_{q=1}^{M} I^{q}(\mathbf{r}), \quad \text{where}$$
 (13)

$$I^{q}(\mathbf{r}) = \int_{\Gamma^{q}} \widetilde{H}(\mathbf{r}, \mathbf{r}') \widetilde{\varphi}(\mathbf{r}') d\sigma(\mathbf{r}'), \tag{14}$$

with

$$\widetilde{H}(\mathbf{r}, \mathbf{r}') = \begin{cases} \frac{\partial G(\mathbf{r}, \mathbf{r}')}{\partial \mathbf{n}(\mathbf{r}')} - ikG(\mathbf{r}, \mathbf{r}'), & \text{(Closed surface),} \\ G(\mathbf{r}, \mathbf{r}'), & \text{(Open surface).} \end{cases}$$
(15)

In the following section we propose a methodology for accurate numerical evaluation of the integrals $I^q(\mathbf{r})$ for a given discrete approximation of the density $\widetilde{\varphi}(\mathbf{r}')$. The solution to the integral equation problem then follows via an application of the iterative linear-algebra solver GMRES.

4. Integration strategy

The integration scheme we present consists of three main components: (1) Use of Fejér's first quadrature rule to compute integrals between patches that are "far" away from each other, (2) A rectangular-polar high-order accurate quadrature rule for self-patch and near-patch singular integrals, and (3) A change of variables that resolves the density singularities that arise at edges.

Using, for each q, the parametrization \tilde{r}^q , the integral (14) can be expressed in the form

$$I^{q}(\mathbf{r}) = \int_{-1}^{1} \int_{-1}^{1} \widetilde{\mathbf{H}}^{q}(\mathbf{r}, s, t) \widetilde{J}^{q}(s, t) \widetilde{\varphi}^{q}(s, t) ds dt, \quad (\mathbf{r} \in \Gamma),$$
(16)

where $\widetilde{J}^q(s,t)$ denotes the surface Jacobian, and where

$$\widetilde{H}^{q}(\mathbf{r}, s, t) = \widetilde{H}(\mathbf{r}, \widetilde{\mathbf{r}}^{q}(s, t)), \tag{17}$$

$$\widetilde{\varphi}^{q}(s,t) = \widetilde{\varphi}\left(\widetilde{\boldsymbol{r}}^{q}(s,t)\right). \tag{18}$$

The strategy proposed for evaluation of the integral in equation (16) depends on the proximity of the point r to the q-th patch Γ^q . For points r that are farther from Γ^q than a certain "proximity distance" $\delta > 0$, Fejér's first quadrature rule is used as detailed in Section 4.2. A special technique, the rectangular-polar method, is then presented in Section 4.3 to treat points whose distance to Γ^q patch is less than or equal to δ . The method we use for selection of specific values of the proximity distance δ is discussed in Section 4.6. Prior to the presentation of these smooth, singular and near-singular integration methods, Section 4.1 describes the singular character of integral-equation densities at edges, and it proposes a methodology, which is incorporated in the subsequent sections, for edge treatment in a high-order accurate fashion.

4.1. Density singularities along edges

The sharp edges encountered in general geometric structures have provided a persistent source of difficulties to integral equation methods and other scattering solvers. The presence of edges leads to (integrable) singularities in the density solutions in both the open-surface [21] and closed-surface [22, 23] cases. The strength of the singularity, however, depends on the formulation and, for closed-surfaces, on the angle at the edge, which is generally not constant.

In order to tackle this difficulty in a general and robust manner, we introduce a change of variables on the parametrization variables (s, t), a number of whose derivatives vanish along edges. Such changes of variables can be devised on the basis of mappings such as the one presented in [9, Sec. 3.5], which is given by

$$w(\tau) = 2\pi \frac{[\nu(\tau)]^p}{[\nu(\tau)]^p + [\nu(2\pi - \tau)]^p}, \quad 0 \le \tau \le 2\pi,$$
(19)

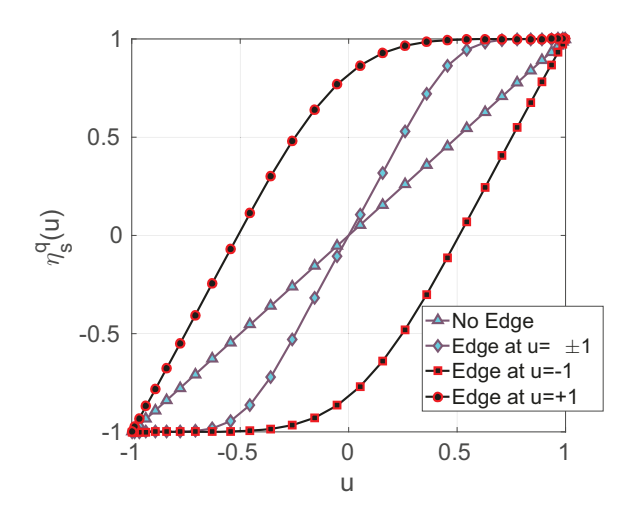


Fig. 1: Changes of variables (equations (21) and (22)) used to resolve edge-singularities in the density.

where

$$v(\tau) = \left(\frac{1}{p} - \frac{1}{2}\right) \left(\frac{\pi - \tau}{\pi}\right)^3 + \frac{1}{p} \left(\frac{\tau - \pi}{\pi}\right) + \frac{1}{2}.$$
 (20)

It is easy to check that the derivatives of $w(\tau)$ up to order p-1 vanish at the endpoints. The function $w(\tau)$ can then be used to construct a change of variables to accurately resolve the edge singularities while mapping the interval [-1, 1] to itself. The change-of-variable mappings we use are given by

$$s = \eta_s^q(u) = \begin{cases} u, & \text{No edge on } s \\ -1 + \frac{1}{\pi}w(\pi[u+1]), & \text{Edges at } s \pm 1 \\ -1 + \frac{2}{\pi}w(\frac{\pi}{2}[u+1]), & \text{Edge at } s = -1 \text{ only} \\ -3 + \frac{2}{\pi}w(\pi + \frac{\pi}{2}[u+1]), & \text{Edge at } s = 1 \text{ only} \end{cases}$$
 (21)

and similarly

$$t = \eta_t^q(v) = \begin{cases} v, & \text{No edge on } t \\ -1 + \frac{1}{\pi}w \left(\pi[v+1]\right), & \text{Edge at } t \pm 1 \\ -1 + \frac{2}{\pi}w \left(\frac{\pi}{2}[v+1]\right), & \text{Edge at } t = -1 \text{ only} \\ -3 + \frac{2}{\pi}w \left(\pi + \frac{\pi}{2}[v+1]\right), & \text{Edge at } t = 1 \text{ only} \end{cases}$$
(22)

Incorporating the changes of variables (21) and (22), the integral in equation (16) becomes an integral in which a weakly singular kernel is applied to a finitely smooth function:

$$I^{q}(\mathbf{r}) = \int_{-1}^{1} \int_{-1}^{1} \mathbf{H}^{q}(\mathbf{r}, u, v) J^{q}(u, v) \frac{d\eta_{s}^{q}}{du}(u) \frac{d\eta_{t}^{q}}{dv}(v) \varphi^{q}(u, v) du dv, \quad \mathbf{r} \in \Gamma,$$

$$(23)$$

where

$$\mathbf{H}^{q}(\boldsymbol{r},u,v) = \widetilde{\mathbf{H}}^{q}\left(\boldsymbol{r},\eta_{s}^{q}(u),\eta_{t}^{q}(v)\right),\tag{24}$$

$$\varphi^{q}(u,v) = \widetilde{\varphi}^{q}\left(\eta_{s}^{q}(u), \eta_{t}^{q}(v)\right),\tag{25}$$

$$\mathbf{r}^{q}(u,v) = \widetilde{\mathbf{r}}^{q} \left(\eta_{s}^{q}(u), \eta_{t}^{q}(v) \right), \tag{26}$$

$$J^{q}(u,v) = \widetilde{J}^{q}(s,t). \tag{27}$$

(The high-order edge-vanishing factors in the integrand smooth-out any possible edge singularities in the density φ^q [9].) The proposed algorithm evaluates such integrals by means of the "smooth-density methods" described in Sections 4.2 and 4.3 below.

4.2. Non-adjacent integration

The algorithm we use for the evaluation of the quantity $I^q(r)$, defined by (16), is based on the reformulation (23)—which, in view of (21) and (22), takes into account all the possible edge/no-edge combinations that may occur within an integration patch. (The algorithm does assume that geometric singularities may only appear along patch boundaries.)

In the "non-adjacent" integration case considered in this section, in which the point r is at the distance larger than or equal to the proximity distance δ , the integrand in (23) is "sufficiently smooth"—on account of, both, the smoothness of the integral kernel for arguments larger than or equal to δ , as well as the changes of variables inherent in that equation, which, in particular, give rise to edge-vanishing derivative factors that smooth-out any possible edge-singularity in the density φ^q itself. Using well known asymptotics of edge singularities it is easy to check that the vanishing derivatives indeed smooth out all possible edge singularities, to any desired order of smoothness, provided a sufficiently high value of p is used [9]. Values of p as low as p=2 are often found to be adequately useful, for accuracies of the order of 1%. Use of larger values of p, of the orders of four to six or above, can enable significantly faster convergence and lower computing costs for higher accuracies. But use of such values do require special treatment of certain types of Green-function cancellations, as described in [24, Sec. A.3], that occur in the case of the double-layer operator. For simplicity, in the present contribution all such challenges are avoided: only changes of variables (19) with the value p=2 are used, and then, avoiding use of excessively fine meshes—so that the cancellation errors under consideration turn out to be negligible. But the method in [24, Sec. A.3] can be applied in the present context to eliminate all numerical cancellation errors.

In view of the smoothness of the integrands for the non-adjacent case considered presently, then, the integral in (23) can be evaluated accurately on the basis of any given high-order quadrature rule. Our implementation utilizes Fejér's first quadrature rule [25], which effectively exploits the discrete orthogonality property satisfied by the Chebyshev polynomials in the Chebyshev meshes used. The Chebyshev discrete orthogonality property also enables straightforward computation of the two-dimensional Chebyshev transforms that are required as part of the singular and near-singular integration algorithms described in Section 4.3.

For a discretization using N points, the nodes and weights of Fejér's first quadrature rule are given by

$$x_j = \cos\left(\pi \frac{2j+1}{2N}\right), \quad j = 0, \dots, N-1,$$
 (28)

$$w_j = \frac{2}{N} \left(1 - 2 \sum_{\ell=1}^{\lfloor N/2 \rfloor} \frac{1}{4\ell^2 - 1} \cos\left(\ell \pi \frac{2j+1}{N}\right) \right), \quad j = 0, \dots, N-1,$$
 (29)

respectively. Then using the Cartesian-product discretization $\{u_i = x_i | i = 0, \dots, N_u^q - 1\} \times \{v_j = x_j | j = 0, \dots, N_v^q - 1\}$, the integral in (16) can be approximated by the quadrature expression

$$I^{q}(\boldsymbol{r}) \approx \sum_{j=0}^{N_{v}^{q}-1} \sum_{i=0}^{N_{u}^{q}-1} H^{q}(\boldsymbol{r}, u_{i}, v_{j}) J^{q}(u_{i}, v_{j}) \frac{d\eta_{s}^{q}}{du} \frac{d\eta_{t}^{q}}{dv} w_{i} w_{j} \varphi^{q}(u_{i}, v_{j}), \quad \boldsymbol{r} \in \Omega_{q}^{f, \delta}.$$

$$(30)$$

where $\Omega_q^{f,\delta}$ represents the set of points that are at a distance larger than or equal to δ from the q-th integration patch Γ^q .

4.3. Singular "rectangular-polar" integration algorithm and a new edge-resolved integral unknown

Like Section 4.2, the present section concerns the problem of evaluation the quantity $I^q(r)$ on the basis of the reformulation (23). In contrast with Section 4.2, however, the treatment presented here concerns the singular and near-singular cases—in which the evaluation point r is either on the q-th integration patch itself or at a distance smaller than the proximity distance δ from it—wherein the Green function singularity cannot be ignored without compromising accuracy. (The determination of proximity distance values δ is discussed in Section 4.6.) The set of all singular and near-singular points for the q-th patch will be denoted by $\Omega_q^{c,\delta}$. The problem of evaluation of I^q for $r \in \Omega_q^{c,\delta}$ presents a significant challenge in view of the singularity of the kernel $\widetilde{H}(r,r')$ at r=r'.

In order to deal with this difficulty, we utilize once again smoothing changes of variables whose derivatives vanish at the singularity or, for nearly singular problems, at the point in the q-th patch that is closest to the singularity. In

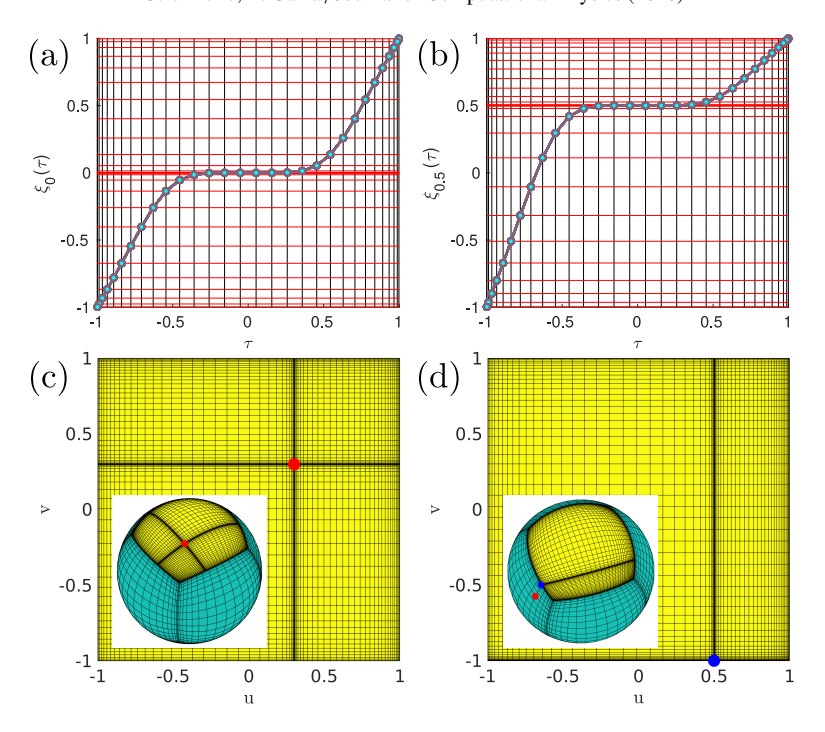


Fig. 2: Figures (a) and (b) show the changes of variables (equation (40)) used to resolve the kernel singularity for two different values of α . Figure (c) presents the mesh, in both parameter and, in inset, real space, produced by the rectangular-polar change of variables to resolve the kernel singularity located at the point marked in red. Figure (d) presents the case for which the target point in red is off-patch from the near source patch (in yellow), with the projection point depicted in blue.

previous implementations [1, 21], such changes of variables required interpolation of the density φ^q from the fixed nodes (u_i, v_j) to the new integration points. The interpolation step, though viable, can amount to a significant portion of the overall cost. We thus propose, instead, use of a precomputation scheme for which integrals of the kernel times Chebyshev polynomials are evaluated with high accuracy (cf. (35)). Since Chebyshev polynomials can easily be evaluated at any point in their domain of definition, this approach does not require an interpolation step. And, since these integrals are independent of the density, they need only be computed once at the beginning of any application of the algorithm, and reused in the algorithm as part of any necessary integration processes in subsequent linear-algebra (GMRES) iterations. Thus, for a given density φ^q , the overall quantity $I^q(r)$ with $r \in \Omega_q^{c,\delta}$ can be computed by first obtaining the Chebyshev expansion

$$\psi^{q}(u,v) \approx \sum_{m=0}^{N_{v}^{q}-1} \sum_{n=0}^{N_{u}^{q}-1} a_{n,m}^{q} T_{n}(u) T_{m}(v), \tag{31}$$

of the modified edge-resolved (smooth) density

$$\psi^{q}(u,v) = \frac{d\eta_{s}^{q}}{du}(u)\frac{d\eta_{t}^{q}}{dv}(v)\varphi^{q}(u,v),$$

and then applying the precomputed integrals for Chebyshev densities.

In detail, the necessary Chebyshev coefficients $a_{n,m}^q$ are given by the relation [26]

$$a_{n,m}^{q} = \frac{\alpha_{n} \alpha_{m}}{N_{u}^{q} N_{v}^{q}} \sum_{i=0}^{N_{v}^{q}-1} \sum_{i=0}^{N_{u}^{q}-1} \psi^{q}(u_{i}, v_{j}) T_{n}(u_{i}) T_{m}(v_{j})$$
(32)

that results from the discrete-orthogonality property enjoyed by Chebyshev polynomials, where

$$\alpha_n = \begin{cases} 1, & n = 0, \\ 2, & n \neq 0. \end{cases}$$
 (33)

As is well known, the Chebyshev coefficients $a_{n,m}^q$ can be computed in a fast manner either by means of the FFT algorithm or, for small expansion orders, by means of partial summation [27, Sec. 10.2]. In practice, relatively small orders and numbers of discretization points are used, and we thus opted for the partial summation strategy.

Using the expansion (31) we then obtain

$$I^{q}(\mathbf{r}) = \int_{-1}^{1} \int_{-1}^{1} \mathbf{H}^{q}(\mathbf{r}, u, v) J^{q}(u, v) \left(\sum_{m=0}^{N_{v}^{q}-1} \sum_{n=0}^{N_{u}^{q}-1} a_{n,m}^{q} T_{n}(u) T_{m}(v) \right) du dv$$
 (34)

from which, exchanging the integrals with the sum, it follows that

$$I^{q}(\mathbf{r}) = \sum_{m=0}^{N_{v}^{q}-1} \sum_{n=0}^{N_{u}^{q}-1} a_{n,m}^{q} \int_{-1}^{1} \int_{-1}^{1} H^{q}(\mathbf{r}, u, v) J^{q}(u, v) T_{n}(u) T_{m}(v) du dv.$$
 (35)

As mentioned above, the double integrals on the right-hand side of this equation are independent of the density: for each q, they only depend on the geometry, the kernel, and the target point $\mathbf{r} \in \Omega_q^{\mathrm{c},\delta}$. For the computation of the forward map, we need, in particular, to evaluate $I^q(\mathbf{r})$ for all discretization points $\mathbf{r} \in \Omega_q^{\mathrm{c},\delta}$. Thus, in the proposed strategy, the integral in (35) must be precomputed for each q and for each combination of a target point $\mathbf{r} \in \Omega_q^{\mathrm{c},\delta}$ and a relevant product of Chebyshev polynomials. Denoting the set of all discretization points by

$$\chi = \left\{ \tilde{r}^{q} \left(\eta_{s}^{q}(u_{i}), \eta_{t}^{q}(v_{j}) \right) \middle| q = 1, \dots, M, \ i = 0, \dots, N_{u}^{q} - 1, \ j = 0, \dots, N_{v}^{q} - 1 \right\},$$
(36)

and using the weights

$$\beta_{n,m}^{q,\ell} = \int_{-1}^{1} \int_{-1}^{1} \mathbf{H}^{q}(\boldsymbol{r}_{\ell}, u, v) J^{q}(u, v) T_{n}(u) T_{m}(v) \, \mathrm{d}u \, \mathrm{d}v, \quad \text{for each } \boldsymbol{r}_{\ell} \in \left\{ \chi \cap \Omega_{q}^{\mathrm{c}, \delta} \right\}, \tag{37}$$

equation (35) becomes

$$I^{q}(\mathbf{r}_{\ell}) = \sum_{m=0}^{N_{v}^{q}-1} \sum_{n=0}^{N_{u}^{q}-1} a_{n,m}^{q} \beta_{n,m}^{q,\ell} .$$
 (38)

We now turn our attention to the accurate evaluation of the integrals in equation (37). The previous method [1] utilizes (in a different context, and without precomputations) a polar change of variables that cancels the kernel singularity and thus gives rise to high-order integration. Reference [1] relies on overlapping parametrized patches and partitions of unity to facilitate the polar-integration step. In the case in which non-overlapping LQ patches are utilized, the use of polar integration requires design of complex quadratures near all patch boundaries [21]. To avoid these difficulties, we propose use of certain "rectangular-polar" changes of variables which, like the edge changes-of-variables utilized in Section 4.2, are based on use of the functions (19)–(20) for suitable values of p.

We thus seek to devise a rectangular-polar integration strategy that can accurately treat the kernel singularity for both the self-patch problem (in which the singularity lies on the integration patch and for which changes of variables should have vanishing derivatives at the target point r_{ℓ}), and the near-singular problem (in which vanishing change-of-variable derivatives should occur at the point in the q-th patch that is closest to the observation point r). To achieve this, it is necessary to consider the value

$$\left(\overline{u}_{\ell}^{q}, \overline{v}_{\ell}^{q}\right) = \underset{(u,v) \in [-1,1]^{2}}{\arg \min} \left| \boldsymbol{r}_{\ell} - \boldsymbol{r}^{q}(u,v) \right|, \tag{39}$$

which can be found by means of an appropriate minimization algorithm. In view of its robustness and simplicity, our method utilizes the golden section search algorithm (see [26, Sec. 10.2]) for this purpose, with initial bounds obtained from a direct minimization over all of the the original discretization points r_{ℓ} in the patch. Relying on the coordinates (39) of the projection point in the near-singular case, and using the same notation $(\bar{u}_{\ell}^q, \bar{v}_{\ell}^q)$ for the coordinates of the singular point in the self-patch problem, the relevant rectangular-polar change of variable can be

constructed on the basis of the one-dimensional change of variables

$$\xi_{\alpha}(\tau) = \begin{cases} \alpha + \left(\frac{\operatorname{sgn}(\tau) - \alpha}{\pi}\right) w\left(\pi|\tau|\right), & \text{for } \alpha \neq \pm 1, \\ \alpha - \left(\frac{1 + \alpha}{\pi}\right) w\left(\pi\left|\frac{\tau - 1}{2}\right|\right), & \text{for } \alpha = 1, \\ \alpha + \left(\frac{1 - \alpha}{\pi}\right) w\left(\pi\left|\frac{\tau + 1}{2}\right|\right), & \text{for } \alpha = -1. \end{cases}$$

$$(40)$$

Figure 2 depicts the rectangular-polar change of variables for α values of (a) 0 and (b) 0.5, as well as the resulting two-dimensional grids for the case where the target point lies in the source patch (c) and when the target point is off-patch (d).

Indeed, a new use of Fejér's first quadrature rule now yields

$$\beta_{n,m}^{q,\ell} \approx \sum_{j=0}^{N_{\beta}^{\nu}-1} \sum_{i=0}^{N_{\beta}^{u}-1} \mathbf{H}^{q} \left(\mathbf{r}_{\ell}, u_{i}^{q,\ell}, v_{j}^{q,\ell} \right) J^{q} \left(u_{i}^{q,\ell}, v_{j}^{q,\ell} \right) T_{n} \left(u_{i}^{q,\ell} \right) T_{m} \left(v_{j}^{q,\ell} \right) \mu_{i}^{u,q,\ell} \mu_{j}^{v,q,\ell} w_{i} w_{j}$$

$$(41)$$

where

$$u_i^{q,\ell} = \xi_{\overline{u}_i^q}(x_i), \quad \text{for } i = 0, \dots, N_{\beta}^u - 1,$$
 (42)

$$v_j^{q,\ell} = \xi_{\bar{v}_\ell^q}(x_j), \quad \text{for } j = 0, \dots, N_\beta^\nu - 1,$$
 (43)

are the new quadrature points, and where

$$\mu_i^{u,q,\ell} = \frac{d\xi_{\bar{u}_\ell}^q}{d\tau}(x_i), \quad \text{for } i = 0, \dots, N_\beta^u - 1,$$
 (44)

$$\mu_j^{\nu,q,\ell} = \frac{d\xi_{\bar{\nu}_\ell^q}}{d\tau} \left(x_j \right), \quad \text{for } j = 0, \dots, N_\beta^\nu - 1, \tag{45}$$

denote the corresponding change-of-variable weights. Using sufficiently large numbers N^u_{β} and N^v_{β} of discretization points along the u and v directions to accurately resolve the challenging integrands, all singular and near-singular problems can be treated with high accuracy under discretizations that are not excessively fine (see Figure 3). For points that are closer than a certain prescribed tolerance, usually of the order 10^{-14} , the kernel values are set to zero to avoid zero denominators.

4.4. Computational cost

Let us now estimate the computational cost for the proposed method, focusing on the adjacent (singular and near-singular) integration problem. (The cost of the non-adjacent interactions arises trivially from a double sum, and can be accelerated by means of either an equivalent source scheme [1, 28] or by a fast multipole approach [29].)

For the purposes of our computing-time estimates, let N denote the maximum of the one dimensional discretization sizes N_u^q and N_v^q over all patches $(1 \le q \le M)$, and let N'_{close} denote the maximum, over all the patches, of the numbers of discretization points that are close to the patch (i.e., that are contained in $\Omega_q^{c,\delta}$), but which are not contained in the q-th patch. Additionally, let $N_\beta^u = N_\beta^v = N_\beta$ denote the number of quadrature points used for singular precomputations. With these notations we obtain the following estimates in terms of the (bounded) integer N (of the order of one to a few tens); the (large, proportional to the square of the frequency, for large frequencies) number M of patches, and the related (bounded) parameters N_β (of the order of one to a few hundreds):

- Cost of precomputations: $O(MN_{\beta}^2N(N^2 + N_{\text{close}}'))$ operations (partial summation).
- Cost of forward map:
 - Chebyshev transform (partial summation): $O(MN^3)$ operations.
 - Singular and near-singular interactions: $O(MN^2(N^2 + N'_{close}))$ operations.
 - Non-adjacent interactions $O((M-1)^2N^4)$ operations (or $O(M^{\alpha}N^4)$) operations with α significantly smaller than two if adequate acceleration algorithms are utilized).

4.5. Patch splitting for large problems

Each patch requires creation and storage of a set of self-interaction weights $\beta_{n,m}^{q,\ell}$, for $q=1,\ldots,M$, $n=1,\ldots,N$, $m=1,\ldots,N$ and $\ell=1,\ldots,N^2$, at a total storage cost of $O(MN^4)$ double-precision complex-valued numbers. Additionally, weights also need to be stored for the N'_{close} near-singular points for each patch, and are dependent on the target point, then the total storage for the singular and near-singular weights is $O(MN^4 + MN^2N'_{\text{close}})$.

In order to eliminate the need to evaluate and store a large number of weights that result as N is increased, it is possible to instead increase the number M of patches—which causes the necessary number of weights to grow only linearly. In these regards it is useful to consider the following rule of thumb: in practice, as soon as the wavelength is accurately resolved by the single-patch algorithm, due to the spectral accuracy of Fejér's first quadrature, only a few additional points per patch are needed to produce accuracies of the order of several digits. In view of the estimates in this and the previous section, parameter selections can easily be made by seeking to optimize the overall computing time given the desired accuracy and available memory.

4.6. Practical determination of the proximity distance δ

As indicated in the introductory paragraphs of Section 4, the specialized singular/near-singular rectangular-polar integration algorithm described in Section 4.3 is only used for evaluation of the integral $I^q(r)$ at points r in the set $\Omega_q^{c,\delta}$ of surface points whose distance to Γ^q is less than or equal to a certain "proximity distance" δ . For surface points r in the (closed) complementary set $\Omega_q^{f,\delta}$, whose distance from Γ^q is greater than or equal to δ , the Fejér-based "smooth integrand" non-adjacent integration algorithm introduced in Section 4.2 is used instead.

Clearly, any value $\delta > 0$ results in a valid overall algorithm for evaluation of $I^q(r)$, but the accuracy and efficiency of the method can be critically affected by the particular selection made for this parameter. Indeed, use of excessively small values of δ would lead to application of the non-adjacent integration rule for functions that are nearly singular—which would result in reduced accuracy. Use of excessively large values of δ , in turn, would cause the singular integration algorithm to be used in the evaluation of integrals with smooth integrands—which could be obtained, with equally high accuracy but much more efficiently by means of the non-adjacent integration approach. (Note that variations in the δ value only affect the computational cost of the precomputation scheme described in Section 4.3: in presence of all the necessary precomputed quantities, the forward-map evaluation cost is independent of the value of δ used.)

Fortunately it is not difficult to obtain reasonable values of the δ parameter for any given scattering surface Γ . Useful values of δ for a spherical scatterer can easily be obtained by quantifying forward-map errors by means of the spherical eigenfunction test method presented in Section 5.1; similar accuracies then result for general surface densities containing frequencies comparable to those in a given eigenfunction test. In presence of such accuracy estimation method, the δ parameter may be obtained by optimization via inspection of the errors resulting for a sequence of selected prospective δ values. The optimal δ values do not vary rapidly with either the frequency or the accuracy-tolerance imposed (values around $\delta = 0.1$ or $\delta = 0.2$ were typically used in the test cases for spherical scatterers), and they can further be used for any given surface—allowing that possible additional corrections of this parameter may be beneficial in particular cases to account for geometric variations in geometric detail. Such optimization corrections could be performed on the basis of accuracy estimates for the foward map algorithm on the given surface, with accuracies determined by means of mesh-resolution studies for representative closed-form integral densities $\widetilde{\varphi}$ (such as, e.g. $\widetilde{\varphi} = U^{\rm inc}$ for the left-hand operator in equation (6)). Additional corrections may also prove advantageous whenever Γ contains geometric singularities such as corners or edges; in such cases the test integral densities used should incorporate singularities of the types known to exist at edges and corners in addition to the oscillatory behavior of the incident field.

Even in absence of any such corrections, however, the δ values obtained by the spherical-eigenfunction method have been found widely applicable and can reliably be utilized in absence of additional geometry-related optimizations. For example, all of the numerical results presented in this paper were produced on the basis of the optimized δ parameter value obtained by requiring overall forward-map errors of the order of 10^{-14} for the eigenfunction test problem considered in Section 5.1; use of additionally optimized δ values could have provided somewhat improved efficiency at the expense of additional preparation effort for each problem or group of problems.

5. Numerical results

This section presents a variety of numerical examples demonstrating the effectiveness of the proposed methodology. The particular implementation for the numerical experiments was programmed in Fortran and parallelized using

OpenMP. The runs were performed on a single node of a dual socket Dell R420 with two Intel Xenon E5-2670 v3 2.3 GHz, 128GB of RAM. Unless otherwise stated, all runs where performed using 24 cores. Visualization of the three-dimensional geometries and acoustic fields was done using VisIt [30].

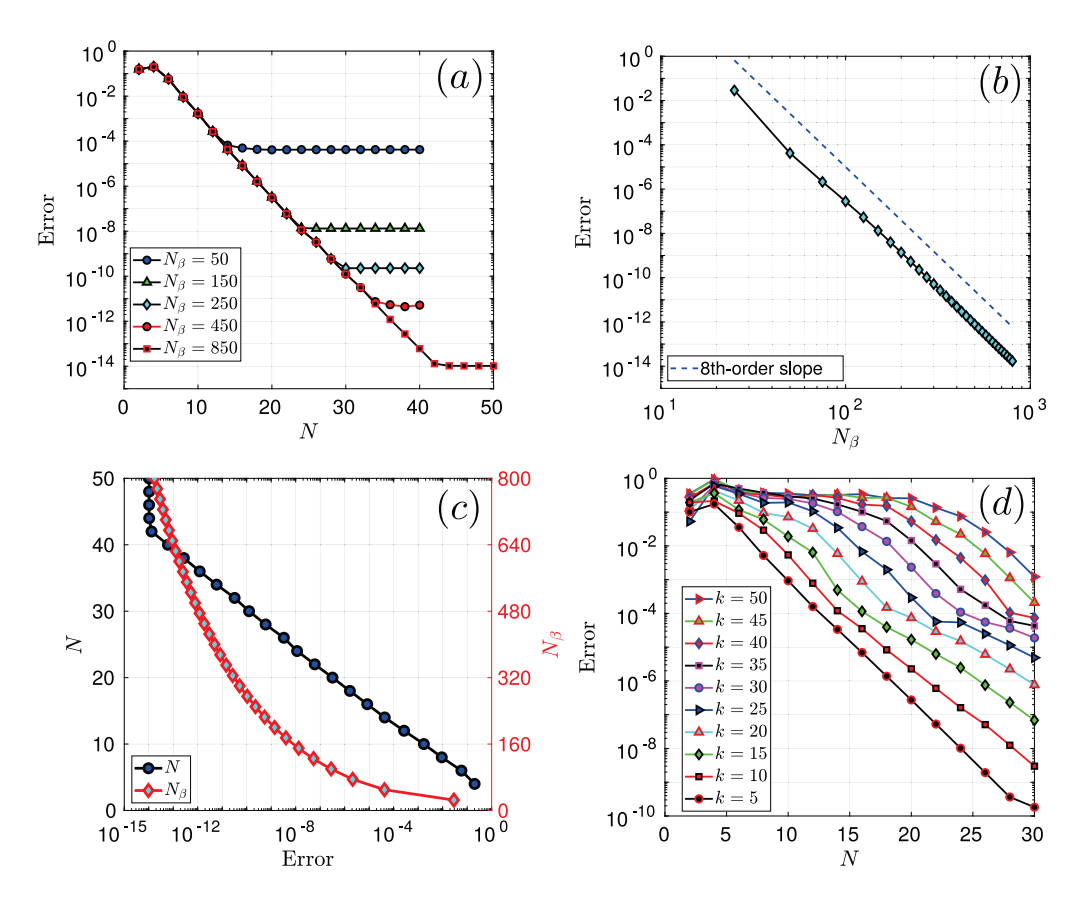


Fig. 3: Forward-map convergence for the combined field formulation over the unit sphere. Figure (a) displays the error as the number N of points per patch per dimension is increased for different values of N_{β} . Figure (b) demonstrates the high-order convergence for the singular integrals as N_{β} is increased. Figure (c) displays the optimal values of N and N_{β} for a given prescribed error. In (a)-(c) $k = 2\pi$. Figure (d) demonstrates the convergence for a range of values of k while keeping the number of patches fixed.

5.1. Performance tests for the spherical scatterer

The accuracy of the overall solver depends critically on the accuracy of the numerical forward map operator, and, accordingly, in this section we first study forward-map errors. In particular, we demonstrate that the proposed methodology yields uniformly accurate evaluations of the action of the integral operator throughout the surface of the scatterer. To do so, we consider the eigenfunctions and eigenvalues of the single- and double-layer operators for Helmholtz equation [31, Sec. 3.2.3]:

$$S[Y_{\ell}^{m}(\theta,\varphi)] = kj_{\ell}(k)h_{\ell}^{(1)}(k)Y_{\ell}^{m}(\theta,\varphi), \tag{46}$$

$$D[Y_{\ell}^{m}(\theta,\varphi)] = \frac{k^{2}}{2} \left[j_{\ell}(k) \frac{\mathrm{d}}{\mathrm{d}k} h_{\ell}^{(1)}(k) + h_{\ell}^{(1)} \frac{\mathrm{d}}{\mathrm{d}k} j_{\ell}(k) \right] Y_{\ell}^{m}(\theta,\varphi), \tag{47}$$

where $j_{\ell}(k)$ and $h_{\ell}^{(1)}(k)$ are the spherical Bessel function of the first kind and spherical Hankel function respectively, and where $Y_{\ell}^{m}(\theta,\varphi)$ are the spherical harmonics. (For the spherical Hankel function $h_{\ell}^{(1)}(z)$ we have used the convention in [31]: $h_{\ell}^{(1)}(z) = -y_{\ell}(z) + i \ j_{\ell}(z)$, where y_{ℓ} is the ℓ -th Neumann function.)

Figure 3 demonstrates the convergence that results as the proposed discrete combined field operator is applied to the spherical-harmonic (5, 2), showing, in particular, that the method is capable of obtaining accuracies close to

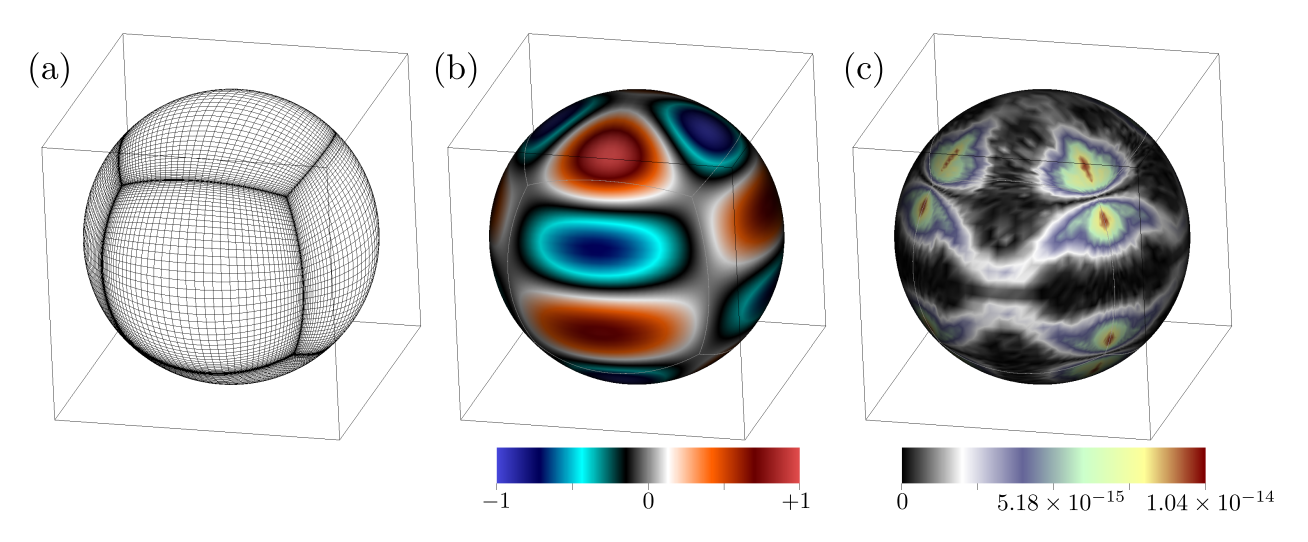


Fig. 4: (a) Mesh, (b) Forward map, and (c) Pointwise error for a (5,2)-spherical-harmonic density using a mesh with N=50 and $N_{\beta}=850$. The error is uniformly close to machine precision.

machine precision in the evaluation of forward maps. Figure 4 displays the spatial distribution of the (near-machine-precision) forward-map error resulting from the discretization described in the figure caption, with errors computed by comparison with the exact result that follows from (46)-(47). It is worth noting that for the double-layer operator, the evaluation of the quantity $n(r') \cdot (r-r')/|r-r'|^2$ is particularly prone to cancellation errors, and to achieve small errors (10⁻⁶ or smaller), special treatment is required. For the particular case of the sphere, the aforementioned quantity can be computed exactly (which is used to obtain the plots in Figure 3), while for more complex geometries, a special treatment based on the curvature of the surface can be used [1].

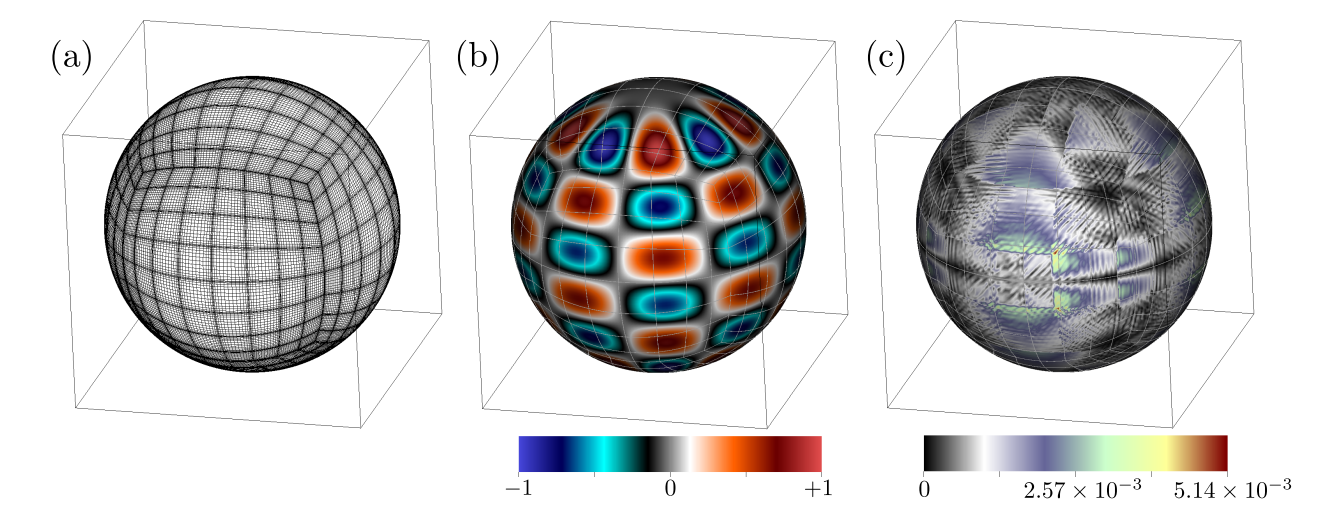


Fig. 5: (a) Mesh, (b) Forward map, and (c) Pointwise error for the (10, 5)-spherical-harmonic density. The figures demonstrate the effect of the patch splitting strategy for high frequencies. In this case k = 100 which corresponds to scattering by a sphere 31.8λ in diameter, using $6 \times 8 \times 8$ patches (8×8 subpatches in each one of 6 initial patches) with N = 14.

As indicated in Section 4.5, for high-frequency problems it is beneficial to split the patches into smaller ones rather than increasing the numbers of points per patch, given that the storage only grows linearly as the number of patches is increased while keeping the number of points per patch constant. In order to determine the optimal balance between accuracy and efficiency, it must be considered that there are two factors that determine the accuracy of the method: (1) The order *N* of the Chebyshev expansions used (i.e. the number of points per patch per dimension), and (2) The

number of points per wavelength. Figure 5 displays the pointwise error in the forward map for a high frequency case. Table 1 presents results for a sphere-scattering problem under several simple patch-splitting configurations. The number of points per wavelength reported in this table is calculated by means of the formula

Points per
$$\lambda = \frac{N}{L/\lambda}$$
, (48)

where $L^2 = 4\pi/M$ denotes the average area of the M quadrilateral patches on the sphere. Clearly the method rapidly produces very high accuracies for small numbers of points-per-wavelength. Table 2 presents results for a range of values of the wavenumber, demonstrating in particular that, as suggested in Section 2.1, for the second-kind formulation we use, the number of iterations required by the GMRES solver to meet a given tolerance remains essentially bounded as k increases. Table 3, finally, demonstrates the solution's convergence to an error less than $10^{-6}\%$, as the numbers of points per wavelength are increased for a fixed set of patches.

N	N_{β}	Patches	Points per λ	Unknowns	Time (prec.)	Time (1 iter.)	GMRES Iter.	Error
8	50	$6 \times 5 \times 5$	1.7	9,600	1.09 s	0.17 s	76	19.3%
12	60	$6 \times 5 \times 5$	2.6	21,600	2.05 s	0.83 s	41	13.4%
16	80	$6 \times 5 \times 5$	3.5	38,400	5.175 s	2.88 s	34	3.80%
8	50	$6 \times 10 \times 10$	3.5	38,400	16.5 s	2.74 s	37	2.92%
12	70	$6 \times 10 \times 10$	5.2	86,400	24.93 s	13.51 s	30	0.111%
16	90	$6 \times 10 \times 10$	6.9	153,600	58.87 s	42.23 s	27	0.00251%

Table 1: Errors in the far field (relative to the maximum far field value) for the solution of scattering by a sphere of diameter 31.8 λ . (The GMRES tolerance was set to 1×10^{-6} .) All computing times reported correspond to runs on 24 computing cores.

k	N	Patches	Points per λ	Unknowns	Time (prec.)	Time (1 iter.)	GMRES Iter.	Error
1.0	8	$6 \times 1 \times 1$	34.7	384	0.06 s	< 0.01 s	7	0.0039%
10.0	10	$6 \times 2 \times 2$	8.7	2,400	0.23 s	0.01 s	13	0.057%
25.0	14	$6 \times 3 \times 3$	7.3	10,584	1.13 s	0.21 s	16	0.0070%
50.0	16	$6 \times 5 \times 8$	6.9	38,400	7.39 s	2.58 s	27	0.0062%
75.0	16	$6 \times 8 \times 8$	7.4	98, 304	30.25 s	17.21 s	21	0.0030%
100.0	16	$6 \times 10 \times 10$	6.9	153,600	68.85 s	42.14 s	22	0.0026%

Table 2: Number of GMRES iterations and other parameters as a function of the wavenumber for the scattering by a unit sphere. (The GMRES tolerance was set to 1×10^{-5} .) A fixed value of $N_{\beta} = 100$ was used in all cases considered in this table, and the patch splitting and values of N_{β} where chosen to keep the number of points per λ close to eight (except for the case k = 1 for which, in order to resolve the geometry itself, a larger number of points per λ was used.).

N	Points per λ	Unknowns	Time (prec.)	Time (1 iter.)	GMRES Iter.	Error
10	6.91	600	0.25 s	< 0.01 s	28	$1.43 \times 10^{0}\%$
15	10.36	1,350	0.50 s	< 0.01 s	26	$4.84 \times 10^{-2}\%$
20	13.82	2,400	1.56 s	0.01 s	25	$1.30 \times 10^{-3}\%$
25	17.27	3,750	2.78 s	0.02 s	23	$1.31 \times 10^{-4}\%$
30	20.73	5,400	10.07 s	0.04 s	23	$4.69 \times 10^{-6}\%$
35	24.18	7,350	25.33 s	0.07 s	23	$8.98 \times 10^{-7}\%$

Table 3: Convergence of the far-field solution for the scattering by a unit sphere $(k = 2\pi/10)$. For this table, the GMRES tolerance was set to 1×10^{-14} , and the original 6 patch configuration (no splitting) was used.

5.2. Edge geometries

As mentioned previously, the important problem of scattering by obstacles containing edges and corners presents a number of difficulties, including density and kernel singularities at the edges. In Figure 6(a) we demonstrate the

performance of the method for a cube geometry, by computing the error in the far field with respect to a reference solution obtained by using a very fine discretization. Figure 7 shows the scattering solution by a cube of side 5λ .

As it can be seen from Figure 6(a), when there is no edge change of variables, the method presents modest convergence rates in the far field solution for the cube. Coarse resolutions don't resolve the densities near the edges properly, but at around 20 points per patch (for this particular case), the error rate settles, and about one digit of accuracy is gained—from 10^{-5} to 10^{-6} —when increasing the discretization from N = 20 to N = 30, i.e. from 2, 400 discretization points to 5, 400. On the other hand, when using the edge change of variables, for coarse resolutions the error is slightly worse given that more points are clustered around the edges, hence not resolving as well the oscillatory nature of the densities in the middle regions of the patches. However, at around 15 points per patch (per dimension), the use of the change of variables leads to better errors. Increasing N from N = 20 to N = 30 results in a decrease in the error by two orders of magnitude, from 10^{-6} to 10^{-8} , where the error for N = 30 is 100 times smaller than the error obtained without the use of edge change of variables.

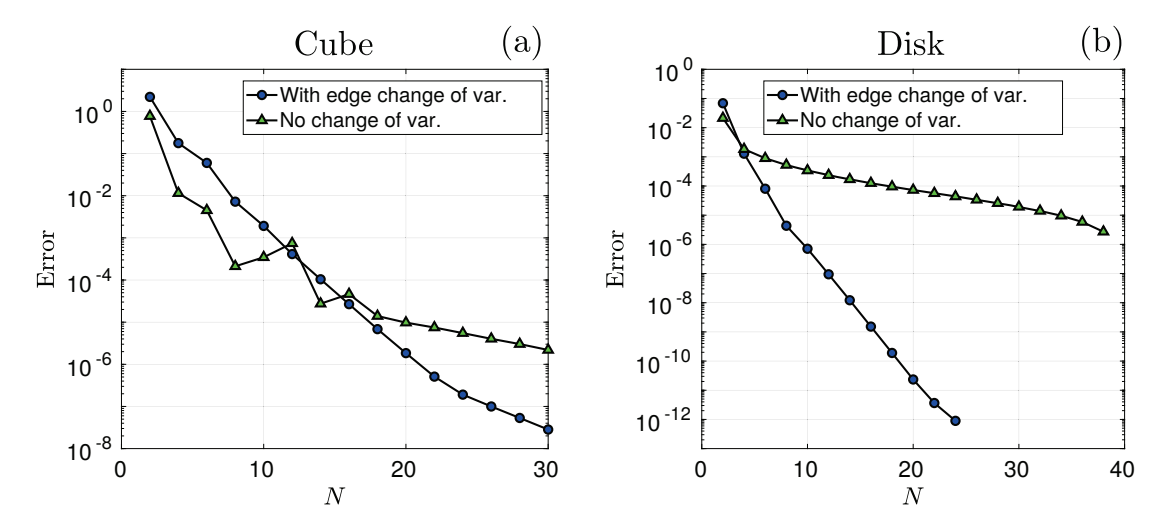


Fig. 6: (a) Maximum (absolute) far-field error for the problem of scattering by a cube of size $2 \times 2 \times 2$ with k = 1. The plot shows results obtained excluding use of an edge change of variables (in green triangles) and including an edge change of variables with p = 2 (in blue circles). The maximum value of the far field for the reference solution equals 2.144. (b) Maximum (absolute) far-field error for the problem of scattering by a disk of radius 1 with k = 1. The plot shows both the curve excluding changes of variables (in green) and including a p = 4 change of variables (in blue). The maximum value of the far field for the reference solution equals 0.7284. In all cases, a sufficiently small GMRES tolerance was used to ensure that accuracy limitations do not arise from a lack of convergence in the GMRES iterative solver.

5.3. Open surfaces

Methods for open surfaces typically suffer from low accuracies, or, alternatively, they require complex treatment at edges. The approach presented here is a straightforward application of the rectangular-polar method, with a change of variables at the edges, as described in Section 4.3. As demonstrated in Figure 6(b), which presents the convergence plot for the far field solution scattered by a disk, the method is robust and high-order accurate. Figure 8 shows the scattering solution for the problem of scattering by a disk 5λ in radius.

Figure 6(b) shows how the use of the edge change of variables leads to a dramatic increase in the convergence rate for the case of open surfaces. Similarly to the case of the cube, a more modest convergence rate results if the change of variables is not employed: increasing N from N = 20 to N = 30 results in a decrease in error by approximately one digit. But an error of 10^{-12} is achieved with N = 22 (a total of 2,420 points) in the case in which the edge change of variables was used. The open surface case benefits more dramatically from the change of variables than the cube, since in this case the change of variables with even powers (which we use), results in *exact cancellation of the density singularity* [21].

5.4. CAD geometries

As indicated in Section 3, CAD designs can be re-expressed as a union of logically-quadrilateral explicitly parametrized patches, and they are thus particularly well suited for use in conjunction with the proposed rectangular-polar solver. To demonstrate the applicability of the solver to such general type of geometry descriptions, Figure 9

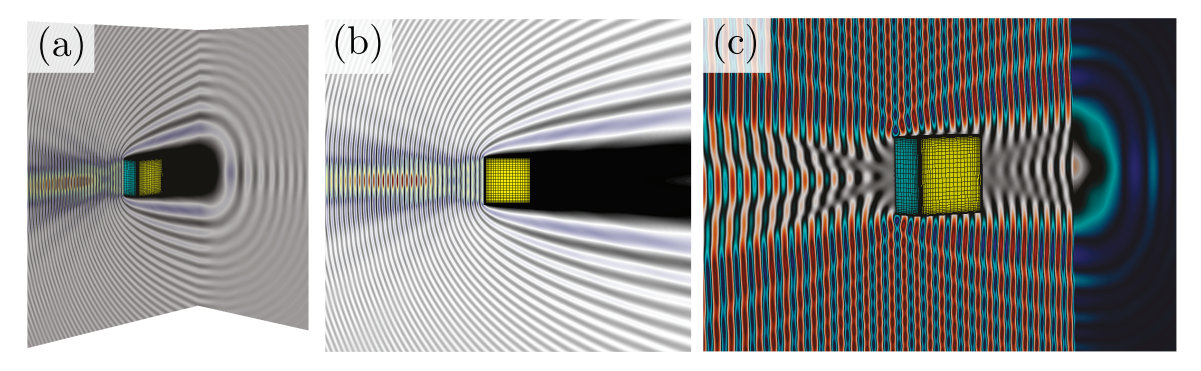


Fig. 7: Scattering by a $5\lambda \times 5\lambda \times 5\lambda$ cube. The intensity profile $|U|^2$ is shown in (a) and (b), while (c) shows the real part of the total field.

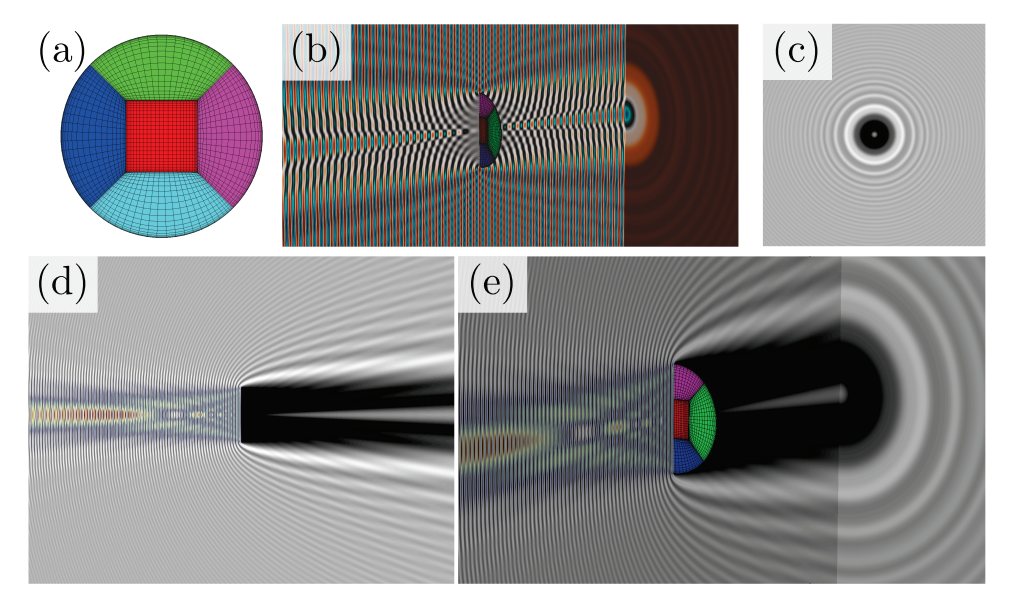


Fig. 8: Scattering by a disk of diameter 10λ with an incident field perpendicular to the disk. Figure (a) displays the patch discretization, Figure (b) presents the real part of the field, and Figures (c)-(e) display three different views of the intensity $|U|^2$. In particular, these figures demonstrate the appearance of the well-known Poisson spot (also known as Arago spot and Fresnel bright spot) clearly visible at the center of Figure (c).

presents a convergence test for the acoustic scattering by a glider CAD design [32] consisting of 148 patches. Figure 10 shows the resulting fields by an incident plane wave incoming from above the glider — in this case, the patches where split into a total of 334 patches to have pairwise similar dimensions and accurately resolve the wavelength. The results in Figure 10 were obtained using a total of 36 GMRES iterations (reaching a residual of 1×10^{-6}). Patch discretizations containing 26×26 points per patch and a value of $N_{\beta} = 80$ were used, leading to a total of 225,784 unknowns. The solution required computing times of 7.2 minutes and 57.42 minutes for the precomputation and GMRES solution (all 36 iterations), respectively. Additionally, the evaluation of the fields on fine (800 × 800) grids over three orthogonal planes required 16.8 minutes.

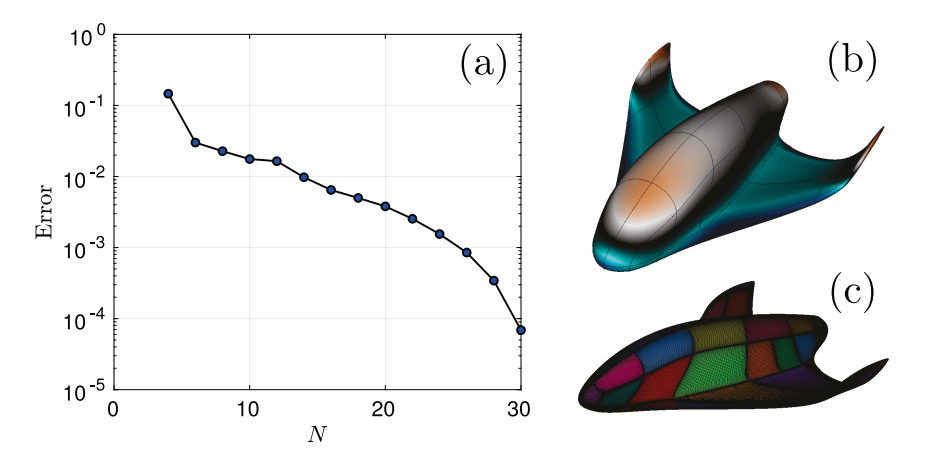


Fig. 9: Figure (a) shows the maximum (absolute) far-field error for the problem of scattering by a glider geometry with k = 1. The reference density solution is shown in (b) and (c) shows the 148 patch discretization. For this convergence test, the longest distance between any two points on the aircraft surface is ~ 2.09 wavelengths, while the wingspan is ~ 1.43 wavelengths.

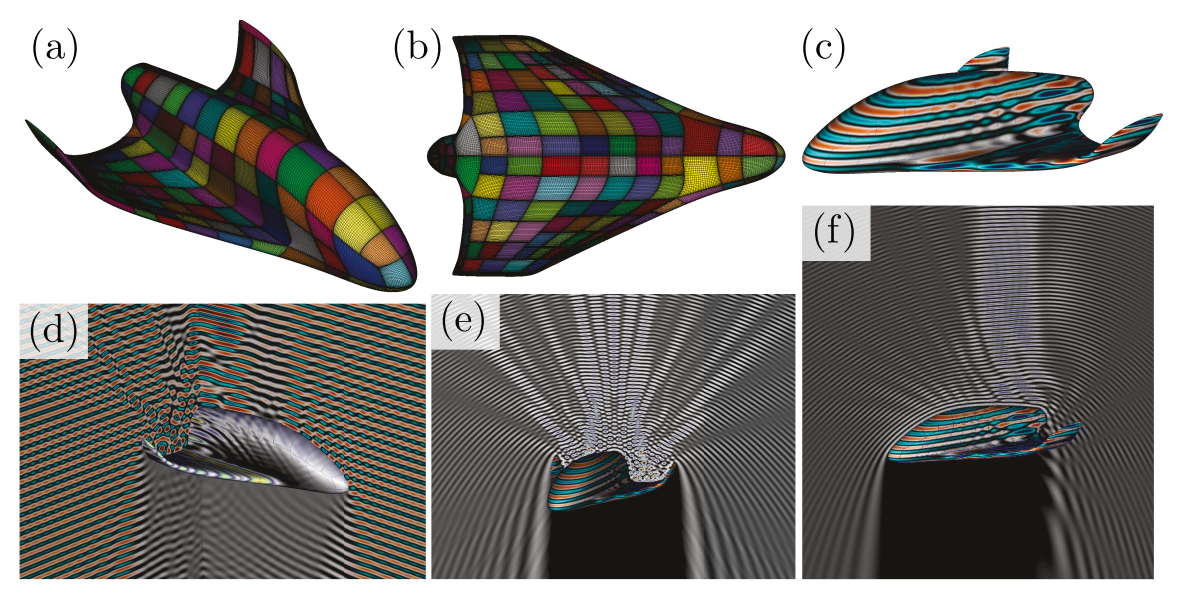


Fig. 10: Scattering by the glider geometry. In this case, $\lambda = 0.5$ which results in about 26 wavelengths from the nose to the tail of the aircraft, and 18 wavelengths across the wingspan. The patches where subdivided to obtain, in all, 334 patches of pairwise similar dimensions. Figures (a) and (b) display the discretization and patch structure of the geometry. The real part of the density is shown in Figure (c). Figure (d) displays the real part of the scattered field along with the absolute value squared of the density at the surface. The intensity of the fields are presented in Figures (e) and (f) for two different view angles.

6. Conclusions

We have presented a rectangular-polar integration strategy for the types of singular kernels that arise in the context of boundary integral equations in scattering theory. The methodology was then used in conjunction with the GMRES linear algebra solver to produce solutions of problems of scattering by obstacles containing open and closed, smooth and non-smooth, scattering surfaces. As demonstrated by a variety of examples presented in Section 5, the overall solver produces results with high-order accuracy, and the rectangular patch description of the geometry makes the algorithm particularly well-suited for application to engineering configurations—where the scattering objects are prescribed in standard (but generally highly complex) CAD representations.

The proposed methodology has been presented in the context of sound-soft acoustic scattering, but the solver can also be used in sound-hard case as well—since kernels can be used in that case [33] that are identical, in character, to the ones we have considered in the present contribution. Preliminary results have shown that this solver is also suitable for electromagnetic scattering in both the PEC and dielectric cases. The numerical examples presented in this paper suggest that the proposed methodology affords a fast, accurate and versatile high-order integration and solution methodology for the problem of scattering by arbitrary engineering structures which, when combined with appropriate acceleration methods, should result in an accurate solver for highly complex, electrically or acoustically large problems of propagation and scattering.

Acknowledgements

The authors gratefully acknowledge support by NSF, AFOSR and DARPA through contracts DMS-1714169 and FA9550-15-1-0043 and HR00111720035, and the NSSEFF Vannevar Bush Fellowship under contract number N00014-16-1-2808. Additionally, the authors thank Dr. Edwin Jimenez and Dr. James Guzman for providing the processing of the CAD geometry used in Section 5.4.

References

- [1] O. P. Bruno, L. A. Kunyansky, A Fast, High-Order Algorithm for the Solution of Surface Scattering Problems: Basic Implementation, Tests, and Applications, Journal of Computational Physics 169 (2001) 80–110.
- [2] M. Ganesh, I. Graham, A high-order algorithm for obstacle scattering in three dimensions, Journal of Computational Physics 198 (2004) 211–242.
- [3] J. Bremer, Z. Gimbutas, A Nyström method for weakly singular integral operators on surfaces, Journal of Computational Physics 231 (2012) 4885–4903
- [4] A. Klöckner, A. Barnett, L. Greengard, M. O'Neil, Quadrature by expansion: A new method for the evaluation of layer potentials, Journal of Computational Physics 252 (2013) 332–349.
- [5] C. Pérez-Arancibia, L. M. Faria, C. Turc, Harmonic density interpolation methods for high-order evaluation of laplace layer potentials in 2d and 3d, Journal of Computational Physics 376 (2019) 411–434.
- [6] C. Pérez-Arancibia, C. Turc, L. Faria, Planewave density interpolation methods for 3d helmholtz boundary integral equations, arXiv preprint arXiv:1901.07437 (2019).
- [7] E. Martensen, Über eine methode zum räumlichen neumannschen problem mit einer anwendung für torusartige berandungen, Acta mathematica 109 (1963) 75–135.
- [8] R. Kußmaul, Ein numerisches verfahren zur lösung des neumannschen außenraumproblems für die helmholtzsche schwingungsgleichung, Computing 4 (1969) 246–273.
- [9] D. Colton, R. Kress, Inverse Acoustic and Electromagnetic Scattering Theory, Springer, New York, third edition, 2013.
- [10] C. Turc, A. Anand, O. Bruno, J. Chaubell, Efficient solution of three-dimensional problems of acoustic and electromagnetic scattering by open surfaces, in: Proceedings of WAVES 2011.
- [11] P. R. Johnston, D. Elliott, A sinh transformation for evaluating nearly singular boundary element integrals, International Journal for Numerical Methods in Engineering 62 (2005) 564–578.
- [12] B. M. Johnston, P. R. Johnston, D. Elliott, A sinh transformation for evaluating two-dimensional nearly singular boundary element integrals, International Journal for Numerical Methods in Engineering 69 (2007) 1460–1479.
- [13] O. P. Bruno, M. Lyon, C. Pérez-Arancibia, C. Turc, Windowed Green Function Method for Layered-Media Scattering, SIAM Journal on Applied Mathematics 76 (2016) 1871–1898.
- [14] O. P. Bruno, C. Pérez-Arancibia, Windowed Green function method for the Helmholtz equation in the presence of multiply layered media, Proceedings of the Royal Society A: Mathematical, Physical and Engineering Science 473 (2017) 20170161.
- [15] C. Pérez-Arancibia, Windowed integral equation methods for problems of scattering by defects and obstacles in layered media, Ph.D. thesis, California Institute of Technology, Applied and Computational Mathematics, Pasadena, CA, USA, 2016.
- [16] O. P. Bruno, E. Garza, C. Pérez-Arancibia, Windowed Green Function Method for Nonuniform Open-Waveguide Problems, IEEE Transactions on Antennas and Propagation 65 (2017) 4684–4692.
- [17] O. P. Bruno, V. Domínguez, F.-J. Sayas, Convergence analysis of a high-order Nyström integral-equation method for surface scattering problems, Numerische Mathematik 124 (2013) 603–645.
- [18] G. A. Chandler, I. G. Graham, Product Integration-Collocation Methods for Noncompact Integral Operator Equations, Mathematics of Computation 50 (1988) 125.
- [19] J. Elschner, The double-layer potential operator over polyhedral domains II: Spline Galerkin methods, Mathematical Methods in the Applied Sciences 15 (1992) 23–37.
- [20] A. Rathsfeld, Nyström's Method and Iterative Solvers for the Solution of the Double-Layer Potential Equation over Polyhedral Boundaries, SIAM Journal on Numerical Analysis 32 (1995) 924–951.
- [21] O. P. Bruno, S. K. Lintner, A high-order integral solver for scalar problems of diffraction by screens and apertures in three-dimensional space, Journal of Computational Physics 252 (2013) 250–274.
- [22] M. Costabel, M. Dauge, General edge asymptotics of solutions of second-order elliptic boundary value problems I, Proceedings of the Royal Society of Edinburgh: Section A Mathematics 123 (1993) 109–155.

- [23] J. Markkanen, P. Ylä-Oijala, A. Sihvola, Surface integral equation method for scattering by DB objects with sharp wedges, Applied Computational Electromagnetics Society Journal 26 (2011) 367–374.
- [24] O. P. Bruno, J. S. Ovall, C. Turc, A high-order integral algorithm for highly singular PDE solutions in Lipschitz domains, Computing 84 (2009) 149–181.
- [25] J. Waldvogel, Fast Construction of the Fejér and Clenshaw-Curtis Quadrature Rules, BIT Numerical Mathematics 46 (2006) 195–202.
- [26] W. H. Press, S. A. Teukolsky, W. T. Vetterling, B. P. Flannery, Numerical recipes: the art of scientific computing, Cambridge University Press, New York, third edition, 2007.
- [27] J. P. Boyd, Chebyshev and Fourier Spectral Methods, Dover Publications, Inc., Mineola, New York, second edition, 2001.
- [28] O. P. Bruno, L. A. Kunyansky, Surface scattering in three dimensions: an accelerated high-order solver, Proceedings of the Royal Society A: Mathematical, Physical and Engineering Sciences 457 (2001) 2921–2934.
- [29] N. A. Gumerov, R. Duraiswami, Fast multipole methods for the Helmholtz equation in three dimensions, Elsevier, San Diego, first edition, 2004.
- [30] H. Childs, E. Brugger, B. Whitlock, J. Meredith, S. Ahern, D. Pugmire, K. Biagas, M. Miller, C. Harrison, G. H. Weber, H. Krishnan, T. Fogal, A. Sanderson, C. Garth, E. W. Bethel, D. Camp, O. Rübel, M. Durant, J. M. Favre, P. Navrátil, VisIt: An End-User Tool For Visualizing and Analyzing Very Large Data, in: High Performance Visualization–Enabling Extreme-Scale Scientific Insight, CRC Press, 2012, pp. 357–372.
- [31] J.-C. Nédélec, Acoustic and Electromagnetic Equations: Integral Representations for Harmonic Problems, Springer, New York, first edition, 2001.
- [32] T. Frevillier, Suborbital spaceflights, https://grabcad.com/library/suborbital-spaceflights-1, 2015. CAD Geometry.
- [33] O. P. Bruno, T. Elling, C. Turc, Regularized integral equations and fast high-order solvers for sound-hard acoustic scattering problems, International Journal for Numerical Methods in Engineering 91 (2012) 1045–1072.